AGU PUBLICATIONS

JGR

Journal of Geophysical Research: Solid Earth

RESEARCH ARTICLE

10.1002/2013JB010480

Key Points:
- There is difference in gas topology during gas invasion and gas nucleation.
- Capillary pressure-vs.-saturation and krw curves are similar for both processes.
- Relative gas permeability (krg) is slightly lower in nucleation than invasion.

Correspondence to:
J. Jang,
jaewon.jang@wayne.edu

Citation:
Jang, J., and J. C. Santamarina (2014), Evolution of gas saturation and relative permeability during gas production from hydrate-bearing sediments: Gas invasion vs. gas nucleation, *J. Geophys. Res. Solid Earth*, *119*, 116–126, doi:10.1002/2013JB010480.

Received 1 JUL 2013
Accepted 17 DEC 2013
Accepted article online 27 DEC 2013
Published online 27 JAN 2014

Evolution of gas saturation and relative permeability during gas production from hydrate-bearing sediments: Gas invasion vs. gas nucleation

Jaewon Jang[1] and J. Carlos Santamarina[2]

[1]Department of Civil and Environmental Engineering, Wayne State University, Detroit, Michigan, USA, [2]School of Civil and Environmental Engineering, Georgia Institute of Technology, Atlanta, Georgia, USA

Abstract Capillarity and both gas and water permeabilities change as a function of gas saturation. Typical trends established in the discipline of unsaturated soil behavior are used when simulating gas production from hydrate-bearing sediments. However, the evolution of gas saturation and water drainage in gas invasion (i.e., classical soil behavior) and gas nucleation (i.e., gas production) is inherently different: micromodel experimental results show that gas invasion forms a continuous flow path while gas nucleation forms isolated gas clusters. Complementary simulations conducted using tube networks explore the implications of the two different desaturation processes. In spite of their distinct morphological differences in fluid displacement, numerical results show that the computed capillarity-saturation curves are very similar in gas invasion and nucleation (the gas-water interface confronts similar pore throat size distribution in both cases); the relative water permeability trends are similar (the mean free path for water flow is not affected by the topology of the gas phase); and the relative gas permeability is slightly lower in nucleation (delayed percolation of initially isolated gas-filled pores that do not contribute to gas conductivity). Models developed for unsaturated sediments can be used for reservoir simulation in the context of gas production from hydrate-bearing sediments, with minor adjustments to accommodate a lower gas invasion pressure P_o and a higher gas percolation threshold.

1. Introduction

Gas and water permeabilities control gas recovery efficiency and determine the economic development of hydrate-bearing sediments [*Johnson et al.*, 2011; *Minagawa et al.*, 2004, 2007; *Gupta*, 2007; *Kleinberg et al.*, 2003; *Jang and Santamarina*, 2011]. Similar expressions for capillary pressure P_c and permeability k_r as functions of the degree of water saturation S_w are used in the discipline of unsaturated soil behavior, in oil production and in CO_2 injection into water-saturated sediments [*Corey*, 1954; *Brooks and Corey*, 1964; *Stone*, 1970; *van Genuchten*, 1980]. However, the applicability of these equations to gas production from hydrate-bearing sediments may be hindered by inherent differences in the evolution of unsaturation: air invades the medium from a boundary and remains as a continuous phase in unsaturated soils; however, gas comes out of solution and bubbles grow within the sediment during hydrate dissociation. A similar situation takes place during depressurization of gas-saturated liquids, such as seepage downstream of earth dams and gassy flow in oil production. These two unsaturation processes are also referred to as “external gas drive” for gas invasion and “internal gas drive” for the cases of gas nucleation [*Yortsos and Parlar*, 1989; *Poulsen et al.*, 2001; *Nyre et al.*, 2008].

In this study, we explore differences between gas invasion and gas nucleation, the evolution of gas saturation, capillary pressure, and relative permeabilities using both experimental and numerical methods. This study assumes a constant porous network and does not consider the solid mass loss during hydrate dissociation [refer to *Dai and Santamarina*, 2013 for complementary results]. A brief review of previous studies follows.

2. Previous Studies

The development of governing equations for unsaturated soils has centered on changes in capillary pressure as a function of water saturation, the evolution in relative water and gas permeabilities, and ensuing mechanical implications (i.e., effective stress, stiffness, and strength).

Table 1. Capillary Pressure in Hydrate-Bearing Sediments as a Function of Water Saturation[a]

Equation		Factors Used in Hydrate-Bearing Sediment Study					References
		Relative Saturation $\bar{S}$	S_{mxw}	S_{rw}	P_0	m or λ	
van Genuchten [1980]	$P_c = P_0\left[\bar{S}^{\frac{-1}{m}} - 1\right]^{1-m}$	$\bar{S} = \frac{S_w - S_{rw}}{S_{mxw} - S_{rw}}$	1	0.14	nr	0.46	*Gamwo and Liu* [2010]
			nr	nr	0.1 MPa	0.45	*Moridis and Reagan* [2007a]
							Moridis and Reagan [2007b]
			nr	0.19	2 kPa	0.45	*Moridis and Sloan* [2007]
			nr	nr	0.1 MPa	0.45	*Moridis et al.* [2009]
			nr	nr	5 kPa	0.77	*Moridis et al.* [2011]
							Reagan et al. [2010]
			nr	0.19	2 kPa	0.45	*Reagan and Moridis* [2008]
			1	nr	2 kPa	0.45	*Rutqvist and Moridis* [2007]
		$\bar{S} = \frac{S_w - S_{rw}}{1 - S_{rg} - S_{rw}}$	$S_{rg} = 0.5$	0.3	1 kPa	0.45	*Hong and Pooladi-Darvish* [2003]
				0.2			*Uddin et al.* [2008]
Corey [1954]	$P_c = P_0\bar{S}^{\lambda}$	$\bar{S} = \frac{S_w - S_{rw}}{1 - S_{rw}}$	nr	nr	nr	−0.5	*Corey* [1954]
			nr	nr	nr	−0.65	*Liang et al.* [2010]
		$\bar{S} = \frac{S_w - S_{rw}}{1 - S_{rg} - S_{rw}}$	$S_{rg} = 0.1$	0.1	5 kPa	−0.25	*Konno et al.* [2010]

[a]Note: (1) S_{mxw}: maximum water content, S_{rg} and S_{rw}: residual gas and water content, P_0: air entry value, m: van Genuchten equation's fitting parameter; and λ: pore size distribution index. (2) Factors depend on soil type: the finer the soil is, the higher P_0 is. (3) nr: not reported. Note: Compiled m-values range from $m = 0.07$ for very fine-grained soils, to $m = 0.34$ for coarse-grained soils [*Wösten et al.*, 1999 for 5521 samples]. But they are different from values used in hydrate simulations summarized in Table 2.

2.1. Capillarity-Saturation Curve

The capillarity-saturation curve captures the causal link between water saturation and capillary pressure [*Leong and Rahardjo*, 1997; *Fredlund*, 2002; *ASTM D*6836-02, 2008]. Pore throat size distribution, connectivity and spatial correlation, soil fabric, contact angle, and interfacial tension determine the capillarity-saturation curve [*Chan and Govindaraju*, 2004; *Francisca and Arduino*, 2007]. There is hysteresis in wetting and drying; most studies are conducted in drying to minimize experimental difficulties [*Hillel*, 1980] and involve either imposing a gas-water pressure difference or drying the soil specimen under a known relative humidity.

Power law equations capture the capillarity-saturation curve in terms of capillary pressure P_c as a function of relative water saturation $\bar{S}$ [*Fredlund and Xing*, 1994]. Two frequently used models and parameters compiled from published hydrate-bearing reservoir simulation studies are presented in Table 1.

2.2. Relative Permeability

The relative permeability of water k_{rw} (or gas k_{rg}) is the conductivity at a given water saturation S_w (or gas S_g) normalized by the water (or gas) conductivity at 100% water saturation (or gas). The conductivity at the irreducible phase saturation may be used as a reference value [*Jaiswal*, 2004]. Relative water or gas permeability varies as a function of water or gas saturation, and predictive models are intimately related to the capillarity-saturation curve models selected for gas invasion; relative permeability equations and the fitting parameters that have been used in hydrate-bearing reservoir simulations are summarized in Table 2.

2.3. Gas Invasion Vs. Gas Nucleation (External Vs. Internal Gas Drive)

During external drive, gas gradually invades the largest interconnected pores advancing from one boundary into the medium. In contrast, internal gas nucleation takes place at independent pores and results in separate and disconnected bubbles before they coalesce to form continuous gas patches [*Poulsen et al.*, 2001; *Egermann and Vizika*, 2001]. The initial distribution of dissociated gas is spatially correlated with the distribution of the hydrate phase in hydrate-bearing sediments.

3. Experimental Study

Experiments are conducted using a two-dimensional micromodel inside a high-pressure chamber to explore spatial fluid distribution during gas invasion and nucleation. The micromodel is built by photo-fabrication and glass etching to form a well-defined two-dimensional pore structure on the bottom glass plate (opening size $d = 0.4$ mm; thickness $t = 0.3$ mm — Figure 1a); afterward, a smooth glass plate is glued on top. The periphery of the micromodel is left open to allow for radial flow. The micromodel is housed inside a high-pressure chamber ($P_{max} = 20$ MPa). A transparent sapphire window allows the use of time-lapse photography to monitor the evolution of gas formation and water drainage. The experimental configuration is shown in Figure 1b.

Table 2. Relative Permeability Equations — Parameters Used in Published Simulations

Equation		Factors Used in Published Hydrate-Bearing Sediment Studies				References
		$\overline{S}$	S_{rw}	S_{rg}	m	
van Genuchten [1980]	$k_{rw} = \overline{S}^{0.5}\left[1-\left(1-\overline{S}^{1/m}\right)^{m}\right]^{2}$	$\overline{S} = \frac{S_w - S_{rw}}{1-S_{rw}-S_{rg}}$	0.3	0.05	0.45	*Hong and Pooladi-Darvish* [2003]
						Hong and Pooladi-Darvish [2005b]
	$k_{rg} = \sqrt{1-\overline{S}}\left(1-\overline{S}^{1/m}\right)^{2m}$		0.2	0.05	0.45	*Uddin et al.* [2008]
						Hong and Pooladi-Darvish [2005a]
Corey [1954]	$k_{rw} = \overline{S}^{4}$	$\overline{S} = \frac{S_w - S_{rw}}{1-S_{rw}-S_{rg}}$				*Nazridoust and Ahmadi* [2007]
	$k_{rg} = \left(1-\overline{S}\right)^{2}\left(1-\overline{S}^{2}\right)$					
	$k_{rw} = S'_{l,g}4$	$S'_{l,g} = \frac{S_{l,g}}{1-S_h}$				*Tonnet and Herri* [2009]
	$k_{rg} = S'^{2}_{g}\left(1-\left(1-S'_{g}\right)^{2}\right)$					
Modified *Stone* [1970]	$k_{rw} = \left(\frac{S_w - S_{rw}}{1-S_{rw}}\right)^{n_w}$	n_w	n_g	S_{rw}	S_{rg}	
		4.0	4.0	0.20	0.02	*Reagan and Moridis* [2008]
	$k_{rg} = \left(\frac{S_g - S_{rg}}{1-S_{rw}}\right)^{n_g}$	3.0	3.0	0.25	0.02	*Moridis and Kowalsky* [2005]
						Moridis et al. [2007]
		3.6	3.6	0.25	0.02	*Moridis and Reagan* [2007a]
		3.6	3.6	0.25	0.02	*Moridis and Reagan* [2007b]
		4.0	4.0	0.20	0.02	*Moridis and Sloan* [2007]
		4.0	4.0	0.20	0.02	*Rutqvist and Moridis* [2007]
		3.6	3.6	0.25	0.02	
		4.0	4.0	0.20	0.02	*Reagan and Moridis* [2008]
						Rutqvist and Moridis [2009]
		3.6	3.6	0.25	0.02	*Moridis et al.* [2009]
		4.5	–	0.24	–	*Anderson et al.* [2011]
		–	3.2	0	0	
		4.5	–	0.25	–	*Kurihara et al.* [2011]
		–	3.2	0	0	
	$k_{rw} = \left(\frac{S_w - S_{rw}}{1-S_{rg}-S_{rw}}\right)^{n_w}$	–	3.0 or 4.0	0.12	–	*Gupta* [2007]
		3.0	2.0	0.10	0.10	*Konno et al.* [2010]
	$k_{rg} = \left(\frac{S_g - S_{rg}}{1-S_{rg}-S_{rw}}\right)^{n_g}$	0.2	0.4	–	–	*Liang et al.* [2010]

3.1. Gas Invasion Test

The micromodel is saturated with green-dyed water. Air is then introduced through the central port connected to the bottom glass plate using a high-pressure syringe pump. Air invades the water-wet micromodel and gradually forms a preferential air flow path until it percolates to the periphery (Figure 2a). Due to the low ratio between air and water viscosities, air invasion tends to finger in advection-dominated regimes [*Lenormand et al.*, 1988; *Santamarina and Jang*, 2010].

3.2. Gas Nucleation Test

The chamber and micromodel are first subjected to vacuum followed by saturation with CO_2 gas ($P = 1.5$ MPa). Then, the micromodel is inundated with water saturated with dissolved CO_2 using the syringe pump. Finally, the pressure inside the chamber is increased to dissolve any residual CO_2 gas ($P = 2.4$ MPa).

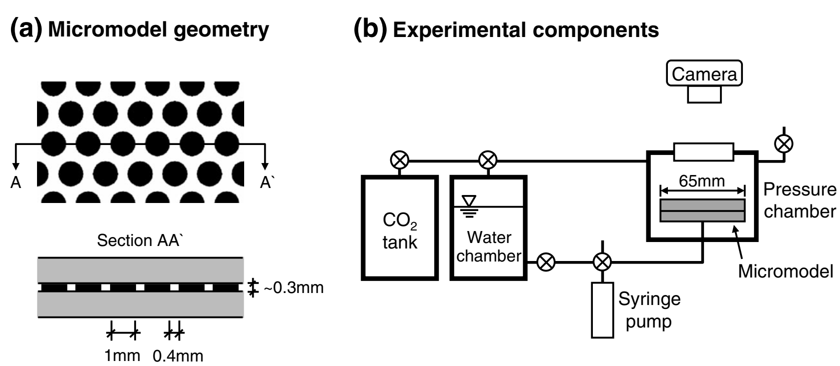

Figure 1. Experimental configuration. (a) Micromodel geometry. (b) Pressure chamber and peripheral components.

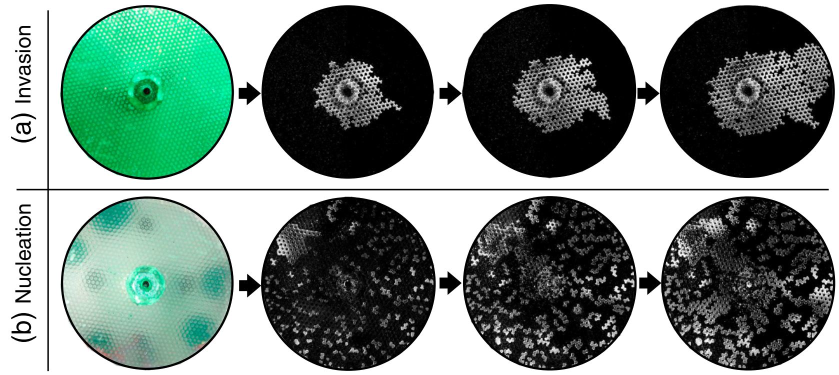

Figure 2. Evolution of gas saturation in micromodels. (a — top row) Gas invasion into water-saturated micromodel. (b — bottom row) Gas nucleation during depressurization of CO_2-saturated water. In both cases, the inlet port is connected at the center of the bottom plate. Image differences are shown to highlight changes with respect to the initial condition shown on the left.

This is the initial, water-saturated condition. The evolution of gas nucleation and water drainage is studied by gradually decreasing the chamber pressure. Time-lapse photography registers the process (Figure 2b). Carbon dioxide comes out of solution and forms isolated gas bubbles throughout the micromodel; eventually, bubbles coalescence and percolate to the periphery. The liquid remains a continuous phase and the liquid pressure is constant throughout the medium under quasi-static conditions; conversely, the gas phase is discontinuous before coalescence, and gas bubbles may have different gas pressures as determined by capillary pressures at pore throats surrounding the gas bubbles [*Jang and Santamarina*, 2011].

3.3. Summary

Experimental results obtained with the porous micromodel highlight profound differences in the gas-distribution morphology during invasion vs. internal nucleation, and hint to higher critical gas saturation when gas percolation is reached by gas nucleation (i.e., internal gas drive). Differences in gas distribution morphology manifest in mechanical properties that are generally proportional to the ratio between capillary pressure and the in situ effective stress, and geophysical parameters [see for example *Dai et al.*, 2012].

4. Numerical Study

A tube-network model is developed to extend the experimental study and to gain insight on the evolution of gas invasion and nucleation processes, and its implications on the capillarity-saturation curves and relative permeabilities.

4.1. Tube-Network Model

Tube-network models consist of tubes connected at nodes (Figure 3a) [*Fatt*, 1956; see also *Blunt*, 2001 for a comprehensive review of network models]. A tube of radius R filled with a wetting fluid at pressure P_w can resist the invasion of a nonwetting gas until the gas pressure P_g reaches the water and capillary pressures combined $P_g > P_w + P_c$. The capillary pressure satisfies Laplace's equation $P_c = 2T_s\cos(\theta)/R$ where T_s is surface tension and θ is the contact angle (Figure 3b).

We use a 3D cubic network for this study (i.e., coordination number 6). Tube radii R are log-normally distributed and the standard deviation in logarithmic scale of tube radius is $\sigma[\ln(R/[\text{mm}])] \approx 0.4 \pm 0.2$ as observed in natural sediments [*Phadnis and Santamarina*, 2011]. Identical network realizations are tested both in gas invasion and in gas nucleation modes.

4.1.1. Simulation Procedure

We assume slow invasion and nucleation so that capillary forces control the evolution of gas and water distribution, that is, both viscous and gravitational forces are disregarded. Gas invasion is enforced at nodes along one boundary plane. On the other hand, gas nucleation is initiated by injecting gas at randomly selected internal nodes to mimic gas generation from hydrate dissociation in sediments. In both cases, the nonwetting gas phase is injected until water no longer drains.

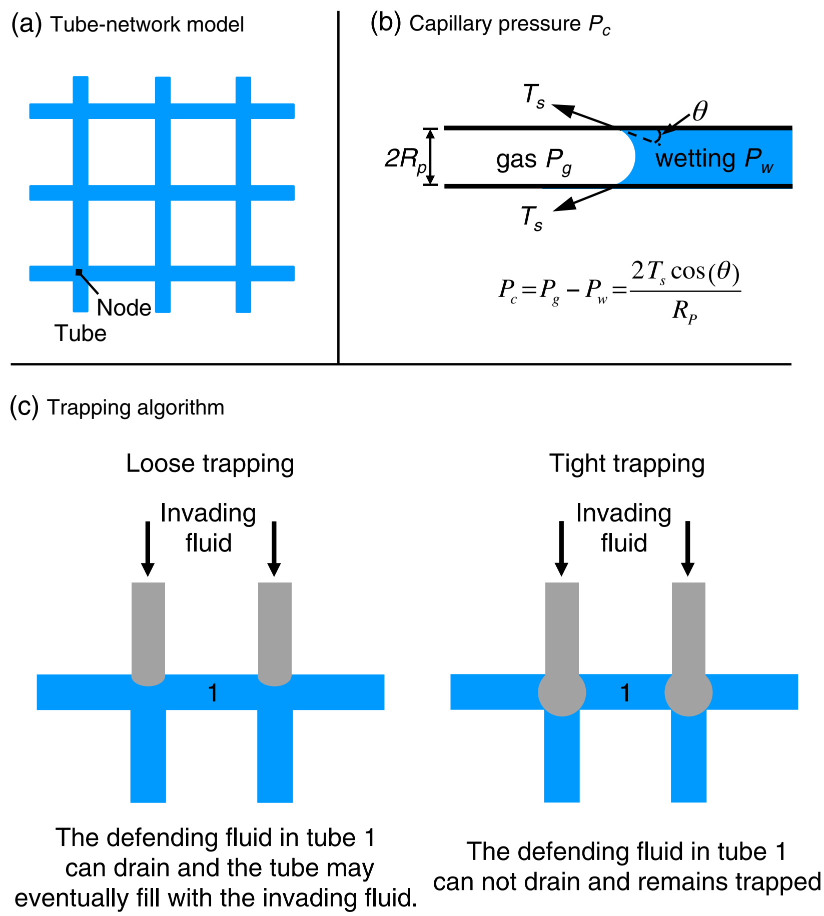

Figure 3. Tube network model: Simulation algorithm. (a) Regular tube geometry: square in 2D and cubic in 3D. (b) Displacement mechanism: the invading gas displaces water as a piston. (c) Trapping algorithm: water in tube #1 is displaced in the "loose trapping" algorithm, but it remains trapped in the tube when the "tight trapping" algorithm is used.

Water may remain trapped in a tube between two air-invaded nodes. Two different trapping hypotheses are considered (Figure 3c). The loose-trapping algorithm assumes that the invading fluid does not occupy nodes; therefore, the water in tube #1 can drain during the invasion process (Figure 3c left). The tight-trapping algorithm assumes that the invading fluid occupies the nodes so that water in an air-bounded tube cannot be drained when gas has invaded both ends (tube #1 in Figure 3c right). Trapping in real sediments falls in between these two extreme cases [*Blunt et al.*, 1992]; in the long-term, water evaporation and vapor pressure equilibration would result in saturation conditions similar to loose trapping. Both algorithms are considered in this study.

The water permeability at a given water saturation is calculated assuming continuity at nodes and zero water transport along gas-filled tubes. Flow is computed using the Hagen-Poiseuille equation; the same method is used for gas permeability assuming zero gas transport along water-filled tubes [see *Jang et al.*, 2011 for details].

4.2. Simulation Results

4.2.1. Effect of Trapping Algorithm

The trapping algorithm impact during gas invasion can be inferred by comparing plots on the left (loose trapping) and right (tight trapping) columns in Figure 4 (three-dimensional tube-network model — network and simulation details in the figure caption). Results show that the capillary-saturation and relative water permeabilities are very similar at high water saturation ($S_w > 0.5$), as are the gas entry pressures P_o. Tight trapping results in higher residual water saturation and lower relative gas conductivity.

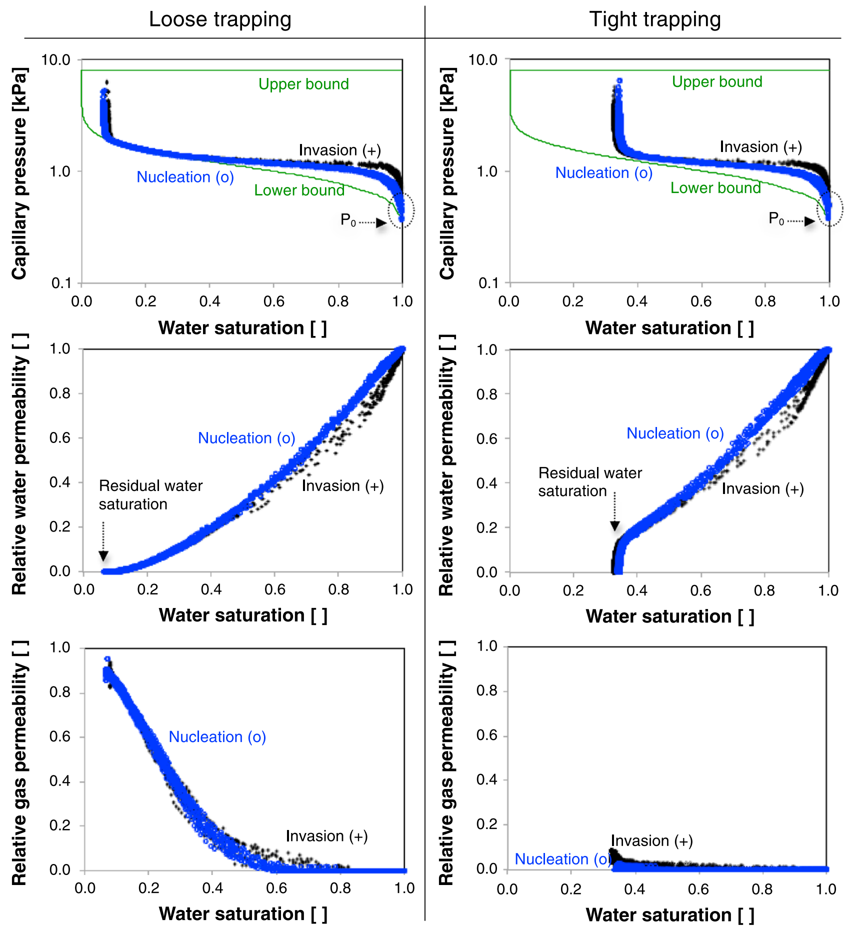

Figure 4. Capillarity-saturation curves and relative permeabilities during gas invasion and internal gas nucleation obtained using the (left column) loose trapping and (right column) tight trapping algorithms. Results from 10 simulations are superimposed in each case. Uncorrelated, three-dimensional tube-network model: 13 × 13 × 13 nodes, 5460 tubes, cubic arrangement with coordination number $cn = 6$, log-normal distribution of tube radius R with mean tube size $\mu(R) = 0.1$ mm, and standard deviation $\sigma(\ln(R/[\text{mm}])) = 0.4$. Parameters for Laplace's equation: $T_s = 72$ mN/m and $\theta = 0°$. Gas invasion: gas is injected at the 13^2 nodes on one boundary. Gas nucleation: gas is injected at 13^2 randomly distributed nodes inside the network.

4.2.2. Capillarity-Saturation Curve

Computed capillarity-saturation curves obtained with loose and tight trapping for spatially uncorrelated randomly distributed tubes are shown in Figures 4 (first row). The gas invasion pressure P_o is higher in invasion than in nucleation.

The bounds for the capillarity-saturation curve are determined by invading the sorted and aligned tubes, starting from the largest tube to obtain the lower bound, or starting from the smallest tube to obtain the upper bound (Figure 4 — top row). All real cases must fall between these two extremes.

4.2.3. Relative Permeability by Gas Invasion and Gas Nucleation

Water and gas permeabilities during gas invasion and nucleation are calculated at every water and gas saturation. Computed conductivities are normalized by the conductivity of the fully saturated network, either $S_w = 1.0$ or $S_g = 1.0$. Results in Figure 4 (middle row) show that water conductivity is slightly lower for gas invasion than for gas nucleation; on the contrary, gas permeability is higher in invasion (Figure 4 — bottom row)

4.2.4. Effect of Spatial Correlation in Tube Size Distribution

The previous simulations were conducted for spatially uncorrelated media. Spatially correlated media exhibit a higher probability of neighboring tubes being of similar size than in a random arrangement of tubes. The effect of spatial correlation in tube size on the capillarity-saturation curve and relative permeabilities is investigated using two-dimensional uncorrelated and correlated networks [20 × 20; correlation length 14 tubes.

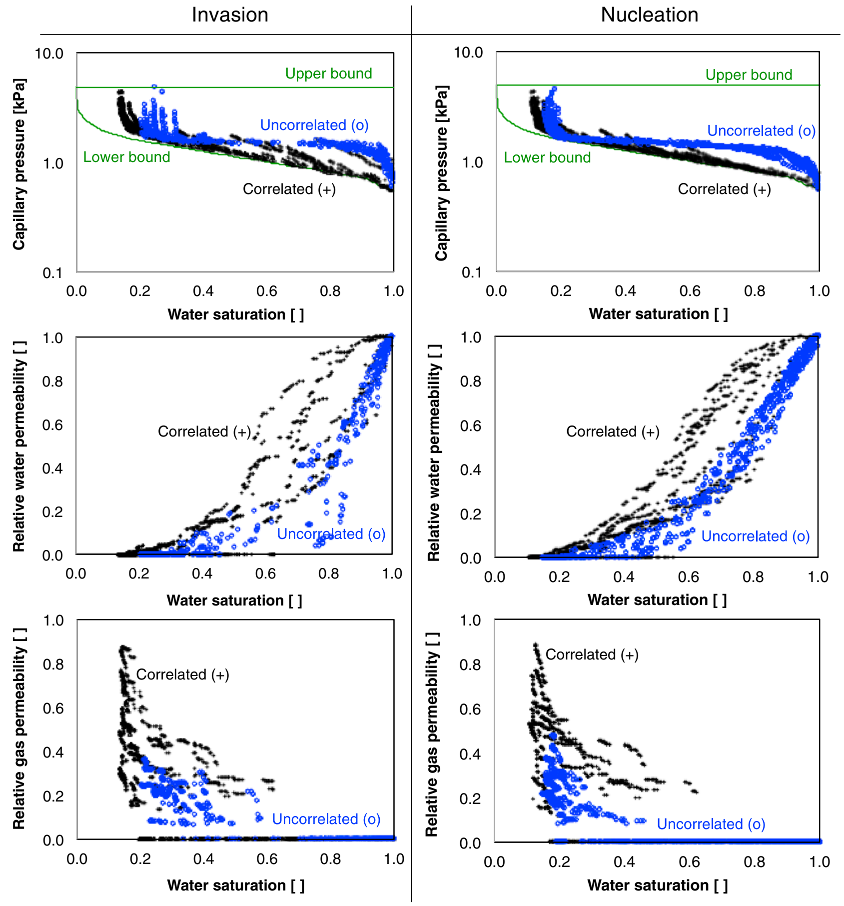

Figure 5. Effect of spatial correlation in tube size distribution on capillarity-saturation curves and relative permeabilities (loose trapping algorithm). Uncorrelated and correlated networks are made of an identical set of tubes; the same number and location of gas injection nodes are used. Two-dimensional network model: square, 20 × 20 nodes, 722 tubes, coordination number $cn = 4$, log-normal distribution of tube radius R with mean tube size $\mu(R) = 0.1$ mm and standard deviation $\sigma(\ln(R/[\text{mm}])) = 0.4$. Parameters for Laplace's equation: $T_s = 72$ mN/m and $\theta = 0°$. Isotropic correlation length is 14 tubes.

Other simulation details in the figure caption. The generation of spatially correlated tube networks is described in *Jang et al.*, 2011]. Results in Figure 5 show that spatial correlation tends to lower the air entry value and capillary-saturation curves move closer to the lower bound; in the meantime, both water and gas relative permeability trends are typically higher for correlated networks than for uncorrelated porous media with the same mean pore size and variance. Gas invasion in spatially correlated media takes place along neighboring large tubes and forms continuous percolating gas paths at relatively low gas saturations compared to the gas invasion in spatially uncorrelated media. Similar differences are observed in the case of gas nucleation as well.

5. Analyses and Discussion

Experimental and numerical results presented above are analyzed in this section to gain physical insight into the evolution of unsaturation and relative permeabilities during gas invasion and nucleation.

5.1. Pore-Scale Observations

In contrast to marked differences in gas distribution morphology, capillarity-water saturation and relative permeability trends are surprisingly similar for gas invasion and gas nucleation. The detailed analysis of the network at selected degrees of saturation shows that the gas-water interface confronts a similar distribution of pore throat sizes whether the gas phase is invading the sediment from the boundary or nucleating at multiple pores within the sediment. Therefore, similar macroscale capillarity-saturation curves are obtained.

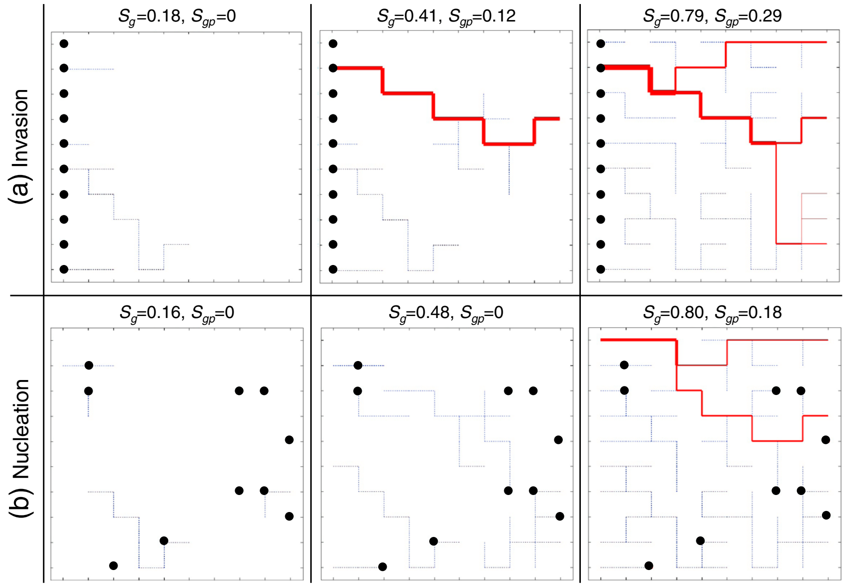

Figure 6. Gas invaded tubes (dotted lines) and percolating gas-filled tubes (continuous lines) at different degrees of saturation during (a) gas invasion and (b) gas nucleation. Note: water-filled tubes are not shown for clarity. Gas injection nodes are shown as solid circles. Line thickness is proportional to gas flow rate. The volume fraction of percolating gas tubes S_{gp} is the ratio of the volume of percolating gas-filled tubes to the volume of all tubes. A small two-dimensional network model is used to facilitate visualization: square, 10 × 10 nodes, 162 tubes, coordination number $cn = 4$, log-normal distribution of tube radius R with the mean tube size $\mu(R) = 0.1$ mm, and standard deviation $\sigma(\ln(R/[\mathrm{mm}])) = 0.4$; tight trapping algorithm. Parameters for Laplace's equation: $T_s = 72$ mN/m and $\theta = 0°$.

Network analyses also reveal hindered coalescence of neighboring gas clusters when water is retained in tight trapping, i.e., short-time invasion [see also *Poulsen et al.*, 2001 in the context of gassy oil].

Differences in gas permeability reflect delayed percolation of gas that nucleates within the medium. This is demonstrated in Figure 6 using a small size network to facilitate the visualization of underlying processes: in this case, the gas phase forms a percolating path from the inlet to the outlet at a gas saturation $S_g = 0.41$ for gas invasion and above $S_g > \sim 0.6$ for nucleation.

5.2. Local Vs. Reservoir-Scale Simulations

Capillarity-water saturation curves and relative permeability trends are local point-properties. Therefore, all computations reported in this study assumed neither gravity nor pressure-temperature-dependent gas viscosity [*Lee et al.*, 1966; *Van der Gulik et al.*, 1988; *Lemmon and Jacobsen*, 2004]. Reservoir scale simulators can account for gravity-driven phase segregation (controlled by the bond number) and changes in viscosity, while keeping capillarity-saturation and relative permeability trends constant for a given homogeneous stratigraphic layer.

5.3. Other Processes — Gassy Oil

Network model simulations and experimental studies conducted to study gas nucleation during oil production (internal gas drive) agree with results presented above and show lower gas permeability than when gas is forced to invade the medium (external gas drive) [*Stewart et al.*, 1954; *Naylor et al.*, 2000; *Poulsen et al.*, 2001; *Yortsos and Parlar*, 1989; *Nyre et al.*, 2008]. Published results also show that pore connectivity, depressurization rate, and pore size distribution affect the critical gas saturation when a gas cluster percolates, the generated gas bubble density, and relative gas permeabilities [*Poulsen et al.*, 2001; *Nyre et al.*, 2008; *Jang and Santamarina*, 2011].

Gas exsolution emerges in other engineered and natural systems, such as: gas bubbles nucleate and gas is released during sea level changes and pockmarks may develop [*Riboulot et al.*, 2013]; gas accumulates and water permeability decreases downstream of dams causing changes in the water pressure and effective stress fields that may trigger instability; gas exsolution during water level decline reduces storage capacity in confined aquifers [*Yager and Fountain*, 2001]; and CO_2 gas can form and migrate after geological CO_2

sequestration due to pressure reduction [*Sakaki et al.*, 2013]. Cyclic hydrological conditions will add complexity to these processes due to the inherent hysterectic nature of capillarity-saturation curves [*Doughty*, 2007].

6. Conclusions

The evolution of capillary pressure and relative permeabilities as a function of water saturation has been extensively studied for gas invasion. The consequences of internal gas nucleation and water drainage are less understood, yet, gas nucleation and bubble growth determine gas flow and recovery during production from hydrate-bearing sediments.

Gas invasion and gas nucleation render very different water and gas distributions: invading gas forms a percolating gas path while nucleating gas forms isolated gas clusters that eventually coalesce into a continuous phase.

In contrast to distinct morphologies in the distribution of liquid and gas phases, numerically computed capillarity-saturation curves are very similar for gas invasion and nucleation, but with higher gas invasion pressure P_o in invasion. Statistically, the gas-water interface at a given degree of saturation confronts a similar distribution of pore throat sizes whether the gas phase is invading the sediment from the boundary or nucleating at multiple pores within the sediment.

The evolution of relative water permeability with saturation shows similar trends in both invasion and nucleation unsaturation processes as well. The mean free path for water flow is not affected by the topology of the gas phase. The evolution of relative gas permeability is more sensitive to the morphology of gas distribution and delayed percolation is anticipated in gas nucleation as isolated gas-filled pores do not contribute to gas conductivity.

Overall, the spatial correlation in pore size emerges as a potentially more important parameter than topological differences that result from gas invasion and gas nucleation.

These results suggest that models developed for unsaturated sediments, such as Corey's and van Genuchten's models, can be used for reservoir simulation in the context of gas production from hydrate-bearing sediments, with minor adjustments to accommodate a lower gas invasion pressure P_o and higher gas percolation thresholds.

Acknowledgments
Support for this research was provided by DOE/NETL Methane Hydrate Project under contract DE-FC26-06NT42963 and the Goizueta Foundation. We are grateful to Dr. H. Huang for insightful comments.

References

Anderson, B. J., et al. (2011), Regional long-term production modeling from a single well test, Mount Elbert gas hydrate stratigraphic test well, Alaska North slope, *J. Mar. Pet. Geol.*, *28*, 493–501.
ASTM D6836-02 (Reapproved 2008), Standard test methods for determination of the soil water characteristic curve for desorption using hanging column, pressure extractor, chilled mirror hydrometer, or centrifuge.
Blunt, M. J. (2001), Flow in porous media – Pore-network models and multiphase flow, *Curr. Opin. Colloid Interface Sci.*, *6*(3), 197–207.
Blunt, M. J., M. J. King, and H. Scher (1992), Simulation and theory of two-phase flow in porous media, *Phys. Rev. A*, *46*(12), 7680–7699.
Brooks, R. H., and A. T. Corey (1964), Hydraulic properties of porous medium, *Hydrology paper No.3*, Civil Engineering Department, Colorado State Univ., Fort Collins, Colo.
Chan, T. P., and R. S. Govindaraju (2004), Estimating soil water retention curve from particle-size distribution data based on polydisperse sphere systems, *Vadose Zone J.*, *3*, 1443–1454.
Corey, A. T. (1954), The interrelation between gas and oil relative permeabilities, *Prod. Mon.*, *19*(1), 38–41.
Dai, S., and J. C. Santamarina (2013), Water retention curve for hydrate-bearing sediments, *Geophys. Res. Lett.*, *40*, 5637–5641, doi:10.1002/2013GL057884.
Dai, S., J. C. Santamarina, W. Waite, and T. Kneafsay (2012), Hydrate Morphology: Patchy Hydrate Saturation in Sands, *J. Geophys. Res.*, *117*, B11205, doi:10.1029/2012JB009667.
Doughty, C. (2007), Modeling geologic storage of carbon dioxide: Comparison of non-hysteretic and hysteretic characteristic curves, *Energy Convers. Manage.*, *48*, 1768–1781.
Egermann, P., and O. Vizika (2001), A new method to determine critical gas saturation and relative permeability during depressurization in the near-wellbore region, *Petrophysics*, *42*(4), 352–361.
Fatt, I. (1956), The network model of porous media, I. Capillary pressure characteristics, *Trans. Am. Inst. Min. Metall. Pet. Eng.*, *207*, 144–159.
Francisca, F. M., and P. Arduino (2007), Immiscible displacement model for anisotropic and correlated porous media, *Int. J. Geomech.*, *7*, 311–317.
Fredlund, D. G. (2002), Use of the soil-water characteristic curve in the implementation of unsaturated soil mechanics, Proceedings of third international conference on unsaturated soils, Recife, Brazil, March, 887–902.
Fredlund, D. G., and A. Xing (1994), Equations for the soil-water characteristic curve, *Can. Geotech. J.*, *31*, 521–532.
Gamwo, I. K., and Y. Liu (2010), Mathematical modeling and numerical simulation of methane production in a hydrate reservoir, *Ind. Eng. Chem. Res.*, *49*, 5231–5245.
Gupta, A. (2007), Methane hydrate dissociation measurements and modeling: The role of heat transfer and reaction kinetics, PhD thesis, Colorado School of Mines.

Hillel, D. (1980), *Fundamentals of Soil Physics*, Academic, San Diego, Calif.

Hong, H., and M. Pooladi-Darvish (2003), A numerical study on gas production from formations containing gas hydrates, Canadian international petroleum conference-54th Annual technical meeting, June 10–12, Calgary, Canada.

Hong, H., and M. Pooladi-Darvish (2005a), Numerical study of constant-rate gas production from in situ gas hydrate by depressurization, in *Scientific Results From the Mallik 2002 Gas Hydrate Production Research Well Program, Mackenzie Delta, Northwest Territories, Canada*, Bulletin, vol. 585, edited by S. R. Dallimore and T. S. Collett, Geological Survey of Canada, St. John's Canada.

Hong, H., and M. Pooladi-Darvish (2005b), Simulation of depressurization for gas production from gas hydrate reservoirs, *J. Can. Pet. Technol.*, *44*(11), 39–46.

Jaiswal, N. J. (2004), Measurement of gas-water relative permeabilities in hydrate systems, MS thesis, University of Alaska, Fairbanks, Alaska.

Jang, J., and J. C. Santamarina (2011), Recoverable gas from hydrate-bearing sediments: Pore network model simulation and macroscale analyses, *J. Geophys. Res.*, *116*, B08202, doi:10.1029/2010JB007841.

Jang, J., G. A. Narsilio, and J. C. Santamarina (2011), Hydraulic conductivity in spatially varying media – A pore-scale investigation, *Geophys. J. Int.*, *184*, 1167–1179.

Johnson, A., S. Patil, and A. Dandekar (2011), Experimental investigation of gas-water relative permeability for gas-hydrate-bearing sediments from the Mount Elbert gas hydrate stratigraphic test well, Alaska north slope, *Mar. Pet. Geol.*, *28*, 419–426.

Kleinberg, R. L., C. Flaum, D. D. Griffin, P. G. Brewer, G. E. Malby, E. T. Peltzer, and J. P. Yesinowski (2003), Deep sea NMR: Methane hydrate growth habit in porous media and its relationship to hydraulic permeability, deposit accumulation, and submarine slope stability, *J. Geophys. Res.*, *108*(10), 2508, doi:10.1029/2003JB002389.

Konno, Y., Y. Masuda, Y. Hariguchi, M. Kurihara, and H. Ouchi (2010), Key factors for depressurization-induced gas production from oceanic methane hydrates, *Energy Fuels*, *24*, 1736–1744.

Kurihara, M., A. Sato, K. Funatsu, H. Ouchi, Y. Masuda, H. Narita, and T. S. Collett (2011), Analysis of formation pressure test results in the Mount Elbert methane hydrate reservoir through numerical simulation, *Mar. Pet. Geol.*, *28*(2), 502–516.

Lee, A. L., M. H. Gonzalez, and B. E. Eakin (1966), The viscosity of natural gases, *J. Pet. Technol.*, *18*(8), 997–1000.

Lemmon, E. W., and R. T. Jacobsen (2004), Viscosity and thermal conductivity equations for nitrogen, oxygen, argon, and air, *Int. J. Thermophys.*, *25*(1), 21–69.

Lenormand, R., E. Touboul, and C. Zarcone (1988), Numerical models and experiments on immiscible displacements in porous media, *J. Fluid Mech.*, *189*, 165–187.

Leong, E. C., and H. Rahardjo (1997), Review of soil-water characteristic curve equations, *J. Geotech. Geoenviron. Eng.*, *123*(12), 1106–1107.

Liang, H., Y. Song, and Y. Chen (2010), Numerical simulation for laboratory-scale methane hydrate dissociation by depressurization, *Energy Convers. Manage.*, *51*, 1883–1890.

Minagawa, H., Y. Hirakawa, M. Sato, R. Ohmura, Y. Kamata, S. Takeya, J. Nagao, T. Ebinuma, H. Narita, and Y. Masuda (2004), Measurement of water permeability under the presence of methane hydrate, AAPG Hedberg research conference, Vancouver, BC, Canada, Sep. 12–16.

Minagawa, H., Y. Nishikawa, I. Ikeda, Y. Sakamoto, T. Komai, and H. Narita (2007), Measurement of methane hydrate sediment permeability using several chemical solutions as inhibitors, The seventh ISOPE ocean mining symposium, Lisbon, Portugal, July 1–6.

Moridis, G. J., and M. B. Kowalsky (2005), Depressurization-induced gas production from class-1 hydrate deposites, SPE Annual Technical Conference and Exhibition, Dallas, TX, ISA, 9–12 Oct., SPE 97266.

Moridis, G. J., and M. T. Reagan (2007a), Strategies for gas production from oceanic class 3 hydrate accumulations, Offshore Technology Conference, OTC 18865, Houston, Tex.

Moridis, G. J., and M. T. Reagan (2007b), Gas production from oceanic class 2 hydrate accumulations, Offshore Technology Conference, Houston, Tex.

Moridis, G. J., and E. D. Sloan (2007), Gas production potential of disperse low-saturation hydrate accumulations in oceanic sediments, *Energy Convers. Manage.*, *48*(6), 1834–1849.

Moridis, G. J., M. Kowalsky, and K. Pruess (2007), Depressurization-induced gas production from class1 hydrate deposits, *SPE Reservoir Eval. Eng.*, *10*(5), 458–481.

Moridis, G. J., M. T. Reagan, S.-J. Kim, Y. Seol, and K. Zhang (2009), Evaluation of the gas production potential of marine hydrate deposits in the Ulleung Basin of the Korea East Sea 2007 SPE Asia Pacific oil&gas conference and exhibition, Jakarta, Indonesia, Oct 30~Nov 1, SPE 110859.

Moridis, G. J., S. Silpngarmlert, M. T. Reagan, T. Collett, and K. Zhang (2011), Gas production from a cold, stratigraphically-bounded gas hydrate deposit at the Mount Elbert gas hydrate stratigraphic test well, Alaska North Slope: Implications of uncertainties, *Mar. Pet. Geol.*, *28*, 517–534.

Naylor, P., T. Fishlock, D. Mogford, and R. Smith (2000), Relative permeability measurements for post-waterflood depressurization of the Miller field, North Sea, SPE annual technical conference and exhibition, Dallas, Texas, October 1~4, SPE 63148, 491–497.

Nazridoust, K., and G. Ahmadi (2007), Computational modeling of methane hydrate dissociation in a sandstone core, *Chem. Eng. Sci.*, *62*, 6155–6177.

Nyre, A. N., S. R. McDougall, and A. Skauge (2008), Effect of depressurization on trapped saturations and fluid flow functions, SPE 16th symposium on improved oil recovery, Tulsa, Okla., April 19~23, SPE 113394, 679–690.

Phadnis, H. S., and J. C. Santamarina (2011), Bacteria in sediments: Pore size effects, *Géotech. Lett.*, *1*(4), 91–93.

Poulsen, S., S. R. McDougall, K. Sorbie, and A. Skauge (2001), Network modeling of internal and external gas drive, International symposium of the society of core analysts, Edinburgh, U.K., Sep., SCA 2001–17.

Reagan, M. T., and G. J. Moridis (2008), Dynamic response of oceanic hydrate deposits to ocean temperature change, *J. Geophys. Res.*, *113*, C12023, doi:10.1029/2008JC004938.

Reagan, M. T., M. B. Kowalsky, G. J. Moridis, and S. Silpngarmlert (2010), The effect of reservoir heterogeneity on gas production from hydrate accumulations in the permafrost, SPE Western Regional Meeting, Anaheim, Calif., 27–29 May.

Riboulot, V., A. Cattaneo, N. Sultan, S. Garziglia, S. Ker, P. Imbert, and M. Voisset (2013), Sea-level change and free gas occurrence influencing a submarine landslide and pockmark formation and distribution in deepwater Nigeria, *Earth Planet. Sci. Lett.*, *375*, 78–91.

Rutqvist, J., and G. J. Moridis (2007), Numerical studies of geomechanical stability of hydrate-bearing sediments, Offshore Technology Conference, Houston, Tex., Apr. 30- May 3.

Rutqvist, J., and G. J. Moridis (2009), Numerical studies on the geomechanical stability of hydrate-bearing sediments, *SPE J.*, *14*(2), 267–282.

Sakaki, T., M. R. Plampin, R. Pawar, M. Komatsu, and T. H. Illangasekare (2013), What controls carbon dioxide gas phase evolution in the subsurface? Experimental observations in a 4.5m-long column under different heterogeneity conditions, *Int. J. Greenhouse Gas Control*, *17*, 66–77.

Santamarina, J. C., and J. Jang (2010), in *Energy Geotechnology: Implications of Mixed Fluid Conditions, Unsaturated Soils*, edited by E. E. Alonso and A. Gens, pp. 33–50, Taylor & Francis Group, London, U. K.

Stewart, C. R., E. B. Hunt, P. N. Schneider, T. M. Geffen, and V. J. Berry (1954), The role of bubble formation in oil recovery by solution gas drives in limestones, *J. Pet. Technol.*, *6*(12), 21–28.

Stone, H. L. (1970), Probability model for estimating three-phase relative permeability, *J. Pet. Technol.*, *22*, 214–218.

Tonnet, N., and J.-M. Herri (2009), Methane hydrates bearing synthetic sediments – Experimental and numerical approaches of the dissociation, *Chem. Eng. Sci.*, *64*, 4089–4100.

Uddin, M., D. Coombe, D. Law, and B. Gunter (2008), Numerical studies of gas hydrate formation and decomposition in a geological reservoir, *J. Energy Resour. Technol.*, *130*, 032,501.

Van der Gulik, P. S., R. Mostert, and V. den Berg (1988), The viscosity of methane at 25C up to 10kbar, *Physica A*, *151*, 153–166.

van Genuchten, M. T. (1980), A closed-form equation for predicting the hydraulic conductivity of unsaturated soils, *Soil Sci. Soc. Am. J.*, *44*, 892–898.

Wösten, J. H. M., A. Lilly, A. Nemes, and C. L. Bas (1999), Development and use of a database of hydraulic properties of European soils, *Geoderma*, *90*, 169–185.

Yager, R. M., and J. C. Fountain (2001), Effect of natural gas exsolution on specific storage in a confined aquifer undergoing water level decline, *Ground Water*, *39*(4), 517–525.

Yortsos, Y. C., and M. Parlar (1989), Phase change in binary systems in porous media: Application to solution-gas drive, SPE annual technical conference and exhibition, SPE 19697, 693–708.